Three-Dimensional Filtering Approach to Brain Potential Mapping

Pei-Chen Lo, *Member, IEEE*

Abstract— The spatial distribution of electroencephalogram (EEG) features on the scalp surface, both in time or frequency, is of great importance in clinical applications and medical research. Traditionally, mathematical methods based on interpolation algorithms have been widely applied to obtain the EEG mappings. This paper presents an innovative approach to reconstructing the brain potential mappings from multichannel EEG's. The three-dimensional (3-D) filtering approach, differing from the numerical interpolating methods, considers the spatial distribution of brain potentials as a 3-D signal, which is processed and interpolated according to its spatial frequency characteristics. The performance of the 3-D filtering method evaluated on simulated brain potentials is shown to be comparable to the four-nearest-neighbors method. Moreover, the 3-D filtering method is superior to the spherical splines method in efficiency. Two main advantages of this method are: the prospect of developing real-time, animated EEG mappings utilizing powerful digital signal processors and its capability of processing and interpolating the brain potentials on the realistic irregular scalp surface.

Index Terms— Brain potential mapping, electroencephalography (EEG), EEG mapping, interpolation methods, multidimensional digital signal, three-dimensional (3-D) digital filter design by frequency transformation method.

I. INTRODUCTION

ELECTROENCEPHALOGRAPHY (EEG) is an important clinical tool for diagnosing and monitoring the nervous system regarding normal or pathological conditions [1], [2]. In the field of EEG study, the spatial or topographical features provide an access to the detection of focal EEG phenomena that have a relationship to focal pathology [1], [2]. The spatial distribution of EEG features (to be called the "EEG mapping" or the "brain mapping") over the scalp surface is thus of great importance. In clinical applications, its graphical display is an easy and straightforward aid to visual inspection of focal activities. A number of methods and techniques have been used for constructing the EEG mapping from a finite number of known values, which are limited by the number of recording electrodes. The quality of brain potential mapping is therefore largely dependent on the interpolation methods and sufficiency of spatial information which involves the number of recording electrodes and sites of electrode placement. In general, a finite number of recording electrodes

(between eight and 25) is used in clinical applications, which limits the spatial resolution. To obtain a better illustration of brain potential distribution, sophisticated processing is required. The EEG mapping has been mostly represented by a two-dimensional (2-D) projection viewed from the vertex (top-view) or from a lateral orientation (side-view) [3]–[6] for decades. Recently, the EEG mapping has utilized advances in computer graphics and mathematical tools, in hopes of providing more aspects regarding the complex brain dynamical mechanism. For example, the 3-D representation of brain potentials on an anatomically realistic head enables visualization of the EEG mappings in every direction [7]–[9], and the spatio-temporal Laplacian field representation simultaneously involves the spatial and temporal characteristics in three-dimensional (3-D) sample space [10].

The interpolation methods developed to construct the EEG mapping are mainly adapted from mathematical (numerical) methods. Among the spatial interpolation algorithms, the four-nearest neighbors (4NN) method [11], [12] presents the advantages of ease of computation and arbitrary electrode locations accompanied, however, by the drawbacks of map discontinuities and extrema located at recording sites [13]. The surface spline interpolation method [13]–[16], another commonly used method, overcomes these drawbacks, yet at the expense of computational complexity. Other interpolation methods [17]–[21] based on approximation and variational techniques focus on fitting the interpolating function to recorded values. Excessive computation time may be required for convergence of the interpolating function to the actual function [20]. These processing methods are basically designed to interpolate and smooth the scalp potential distribution. Filtering is capable of performing the tasks of smoothing and interpolation. Furthermore, the computer technology has been advancing toward the era of multimedia informatics and virtual reality. Researchers in the biomedical engineering field have shown great interest in developing an animated display of EEG mappings evolving with time. Digital filtering technology provides an access to real-time animated brain potential mappings thanks to the efficient realization and implementation in hardware. It is the major motivation for developing this research study.

In the problem of brain potential mapping, we deal with a 3-D digital signal. The fields of multidimensional (MD) digital signal and image processing have become essential during the past two decades [22]. As more research is focused on higher-dimensional signal processing, analysis and interpretation, design of 3-D or even higher-dimensional digital filters is

The author is with the Department of Electrical and Control Engineering, National Chiao Tung University, 1001 Ta-Hsueh Road, Hsinchu, Taiwan, R.O.C. (e-mail: pclo@cc.nctu.edu.tw).

getting more conspicuous and urgent. Applications of 3-D filters could potentially be a prosperous field in many practical problems. Yet the theory of design and implementation of 3-D digital filters is still in its infancy although it has well matured in the two-dimensional (2-D) cases [22]. Intuitively, a few methods for 2-D finite impulse response (FIR) filter design can be straightforwardly adapted for designing higher-dimensional FIR filters with manageable filter characteristics. Problems then occur, such as "what are the appropriate filter specifications" and "how to implement them to perform EEG mapping."

In this paper, we describe an alternative method for constructing the brain potential mapping on the scalp surface. This method, to be called the "3-D filtering method," allows us to implement fast construction of the brain mapping directly from the recorded potential values (raw EEG) or from processed data. Accordingly, it provides a potential tool for real-time display of the brain mapping continuously in the future, which is promised by advances in digital signal processing techniques and hardware technology, such as signal processing chips and microprocessors. In addition, the proposed method is capable of handling any irregular realistic head shape. There is no need to make an assumption of a spherical head shape. As a consequence, it provides an alternative approach to displaying the 3-D EEG mapping on a realistic head model. To explore the feasibility of the 3-D filtering approach for the interpolation and smoothing of the EEG mapping, we require that the performance of this method is comparable to those other commonly used methods. In order to test the performance and make the comparison with the other methods, the spherical current dipole model [23]–[25] is used to simulate the brain potential distribution on the scalp surface. The 3-D filtering approach will be applied to a set of 19, 33, and 45 sampled potential values to construct the EEG mapping. The results are compared with those of the 4NN and spherical splines methods.

This paper is organized as follows: In Section II, we illustrate an approach for designing a 3-D FIR filter. The idea is basically an extension of a 2-D FIR filter designed by the frequency transformation method [26]–[30]. The application of the 3-D filtering method to brain potential mapping is discussed in Section III. Section IV first elaborates on the issue of determining the 3-D filter specifications (mainly the filter bandwidth). Then, its performance is compared to the well-known 4NN and spherical splines interpolation methods. Section IV also evaluates the efficiency of the three methods.

II. DESIGN OF 3-D FILTERS

The frequency transformation method, known as the McClellan transformation [26], is a useful technique for designing 2-D zero-phase or linear-phase nonrecursive filters. Detailed reviews of the 2-D FIR filter design with the McClellan transformation can be found in Lim [22] and Dudgeon and Mersereau [30]. In this section, we discuss in more technical detail the transformation method extended to 3-D FIR filter design and its implementation to brain potential mapping.

The basic idea of the method is to convert a one—dimensional (1-D) zero-phase FIR filter into a 3-D one, through a substitution of frequency variables. The transformation function performs this variable substitution. By using an optimal 1-D filter, one might possibly obtain an optimal 3-D filter if the transformation function is cautiously designed. The design technique involves two strategies: 1) designing a 1-D zero-phase prototype filter which is expressed as an expansion of a Chebyshev polynomial, and 2) designing the transformation function $T(w_1, w_2, w_3)$ which is the discrete-space Fourier transform of a 3-D sequence $t[n_1, n_2, n_3]$.

A. Representation of 1-D Zero-Phase Filters as Chebyshev Polynomials

Let $h[n]$ be the impulse response of an optimally designed 1-D zero-phase filter with length $2N + 1$. Then it must be even symmetric with odd length $(2N + 1)$: $h[n] = h[-n]$, $-N \leq n \leq N$. The frequency response $H(w)$ can be expressed as

$$H(w) = h[0] + \sum_{n=1}^{N} 2h[n] \cos(wn) = \sum_{n=0}^{N} a[n] \cos(wn) \quad (1)$$

where the coefficients $a[n]$ are directly related to the impulse response $h[n]$ and the function $\cos(wn)$ is the nth order Chebyshev polynomial $P_n[\cdot]$ in variable $\cos(w)$. According to the Chebyshev polynomials

$$P_0[\cos(w)] = 1$$
$$P_1[\cos(w)] = \cos(w)$$
$$P_2[\cos(w)] = 2\cos(w)P_1[\cos(w)] - P_0[\cos(w)]$$
$$\vdots$$
$$P_n[\cos(w)] = 2\cos(w)P_{n-1}[\cos(w)] - P_{n-2}[\cos(w)]. \quad (2)$$

The $\cos(wn)$ term in (1) can be substituted by $P_n[\cos(w)]$. The frequency response $H(w)$ then becomes a polynomial of $\cos(w)$

$$H(w) = \sum_{n=0}^{N} b[n][\cos(w)]^n \quad (3)$$

where $b[n]$ can be related to $h[n]$ using (1) and (2). The frequency response $H(w)$ expressed in the form in (3) is ready to be transformed into the frequency response of a 3-D filter, $H(w_1, w_2, w_3)$, with $\cos(w)$ substituted by a function of the 3-D frequency variables, $T(w_1, w_2, w_3)$

$$H(w_1, w_2, w_3) = H(w)|_{\cos(w)=T(w_1, w_2, w_3)}$$
$$= \sum_{n=0}^{N} b[n][T(w_1, w_2, w_3)]^n. \quad (4)$$

$T(w_1, w_2, w_3)$ is the transformation function. From (4), the magnitude of the frequency response at any particular frequency $w = w_i$ will be preserved in $H(w_1, w_2, w_3)$, that is, $|H(w_{1i}, w_{2i}, w_{3i})| = |H(w_i)|$ through the transformation $\cos(w_i) = T(w_{1i}, w_{2i}, w_{3i})$. Accordingly, the 1-D frequencies

are mapped into 3-D surfaces [a set of (w_{1i}, w_{2i}, w_{3i})'s] in the 3-D frequency space. The mapped loci of constant magnitude in the (w_1, w_2, w_3)-space are called isopotentials [30] and the 3-D surfaces created by the transformation $\cos(w_i) = T(w_{1i}, w_{2i}, w_{3i})$ will be called isopotential surfaces. Then the resulting 3-D filter $H(w_1, w_2, w_3)$ evaluated on the isopotential surface equals $H(w_i)$. That is, the magnitude characteristics of $H(w)$ will be preserved in $H(w_1, w_2, w_3)$. It is one of the advantages of the McClellan transformation method. Since values of the 3-D filter $H(w_1, w_2, w_3)$ are directly translated from values of the 1-D prototype filter $H(w)$ on the isopotential surfaces, the shape of isopotential surfaces and frequency characteristics of $H(w)$ are two factors affecting the frequency characteristics of $H(w_1, w_2, w_3)$. Design of the transformation function $T(w_1, w_2, w_3)$ is central to the shape of isopotential surfaces.

B. A 3-D Transformation Function Modified from McClellan's

In the McClellan transformation, it is an essential requirement that $|T(w_1, w_2, w_3)| \leq 1$ since

$$T(w_1, w_2, w_3) = \cos(w). \tag{5}$$

As $T(w_1, w_2, w_3)$ is the discrete-space Fourier transform of a 3-D sequence $t[n_1, n_2, n_3]$, $T(w_1, w_2, w_3)$ can be expressed as

$$T(w_1, w_2, w_3)$$
$$= \sum_{[n_1, n_2, n_3] \in R_t} \sum \sum t[n_1, n_2, n_3] e^{-jw_1 n_1} e^{-jw_2 n_2} e^{-jw_3 n_3} \tag{6}$$

where R_t is the region in the $[n_1, n_2, n_3]$-space that $t[n_1, n_2, n_3] \neq 0$. Hence design of the transformation function $T(w_1, w_2, w_3)$ requires determination of the 3-D sequence $t[n_1, n_2, n_3]$. Normally, R_t is as small as possible in order to minimize the number of nonzero samples of $h[n_1, n_2, n_3]$, impulse response of the 3-D FIR filter. It is shown that for 2-D low-pass filters, a 3×3 square shape is a reasonable selection for R_t [22]. McClellan proposed the transformation function

$$T(w_1, w_2) = -\frac{1}{2} + \frac{1}{2}\cos(w_1) + \frac{1}{2}\cos(w_2)$$
$$+ \frac{1}{2}\cos(w_1)\cos(w_2) \tag{7}$$

which corresponds to a 2-D sequence: $t[0,0] = -1/2$, $t[1,0] = t[0,1] = t[-1,0] = t[0,-1] = 1/4$ and $t[1,1] = t[-1,1] = t[-1,-1] = t[1,-1] = 1/8$. Based on the McClellan transformation function in (7), the resulting 2-D filters have nearly circular isopotential contours in low-frequency regions. However, the deviation from circular symmetry becomes prominent in high-frequency regions. In fact, this does not cause a problem in our application since the brain potential distribution exhibits low spatial frequency characteristics. The circumference of passband region usually does not exceed the frequency regions meeting spherical symmetry in the 3-D FIR filter design. Based on the McClellan transformation for 2-D cases, we derived a 3-D transformation
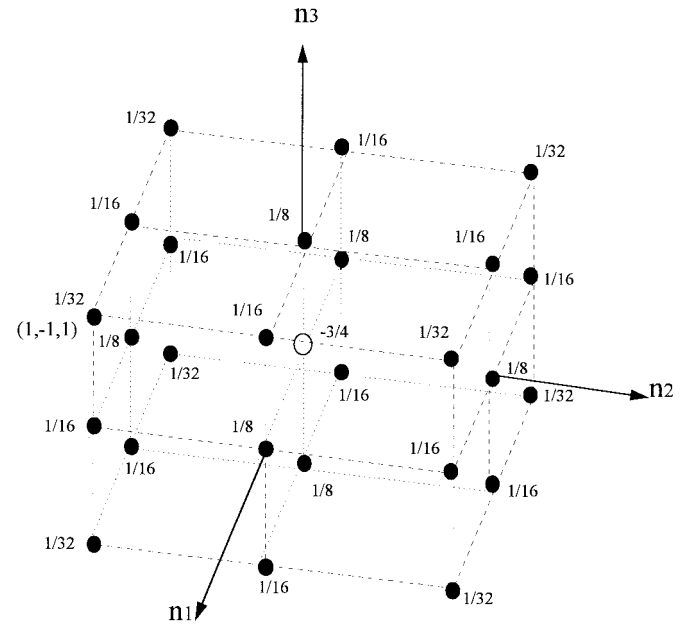

Fig. 1. The 3-D sequence $t[n_1, n_2, n_3]$. Its sample values determine the coefficients in the transformation function $T(w_1, w_2, w_3)$.

function in this study

$$T(w_1, w_2, w_3)$$
$$= -\frac{3}{4} + \frac{1}{4}\cos(w_1) + \frac{1}{4}\cos(w_2) + \frac{1}{4}\cos(w_3)$$
$$+ \frac{1}{4}\cos(w_1)\cos(w_2) + \frac{1}{4}\cos(w_1)\cos(w_3)$$
$$+ \frac{1}{4}\cos(w_2)\cos(w_3) + \frac{1}{4}\cos(w_1)\cos(w_2)\cos(w_3) \tag{8}$$

through which the transformed 3-D low-pass filter possesses spherically symmetric properties in the low-frequency region. The 3-D transformation function in (8) guarantees the maps of 1-D frequencies into 3-D frequency space satisfying

$$\cos(0) = T(0, 0, 0) \tag{9a}$$
$$\cos(\pi) = T(\pi, 0, 0) = T(0, \pi, 0) = T(0, 0, \pi)$$
$$= T(0, \pi, \pi) = T(\pi, 0, \pi) = T(\pi, \pi, 0) = T(\pi, \pi, \pi). \tag{9b}$$

In (9a), we impose the constraint that $w = 0$ be mapped to $(w_1, w_2, w_3) = (0, 0, 0)$, which assumes a 1-D low-pass filter is transformed to a 3-D low-pass filter. The constraint of mappings in high-frequency regions (9b) is not a crucial factor in the designing procedure. In addition, the transformation function in (8) always satisfies the requirement $|T(w_1, w_2, w_3)| \leq 1$ in the entire $2\pi \times 2\pi \times 2\pi$ region. The 3-D sequence $t[n_1, n_2, n_3]$, thus, has a $3 \times 3 \times 3$ region of support (R_t) as shown in Fig. 1. The isopotential surfaces obtained by $\cos(w) = T(w_1, w_2, w_3)$ for the 1-D frequency $w = 0.1\pi$ and 0.5π are plotted in Fig. 2. Only the surface in the hemispace of $w_3 \geq 0$ is shown since the surface is symmetrical with respect to the (w_1, w_2)-plane. Notice that the isopotential surface intersects the w_3-axis at $w_3 = w$ (when $w_1 = w_2 = 0$). It can be well explained from the
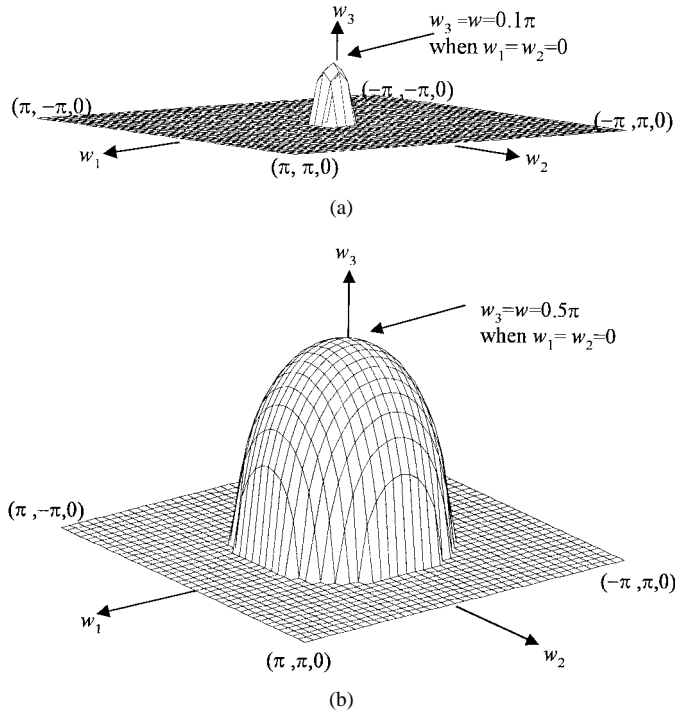
Fig. 2. The isopotential surfaces for (a) $w = 0.1\pi$ and (b) $w = 0.5\pi$.

transformation function evaluated at $w_1 = w_2 = 0$ which gives $\cos(w) = T(0,0,w_3) = \cos(w_3)$. Likewise, the surface intersects the w_1- and w_2-axis at $w_1 = w$ and $w_2 = w$, respectively.

With a given $t[n_1, n_2, n_3]$, the designing strategy was reduced to the translation of the 3-D filter specification to the specification of the 1-D prototype $H(w)$. The $H(w)$ was designed to meet the filter specification by using the optimal 1-D filter design technique developed by Parks and McClellan [31], [32]. From $t[n_1, n_2, n_3]$ and $h[n]$, a 3-D filter $h[n_1, n_2, n_3]$ was obtained by using (1) and (4).

C. A Design Example

Following the filter design concept described above, we use a specific example to illustrate the design procedure. Consider the filter specification for a spherically symmetric 3-D low-pass filter

$$\delta_p \text{ (passband tolerance)} = 0.134 \qquad (10a)$$

$$\delta_s \text{ (stopband tolerance)} = 0.030 \qquad (10b)$$

$$\|\overrightarrow{w}_p\| = 0.08\pi \text{ (passband cutoff frequency)} \qquad (10c)$$

$$\|\overrightarrow{w_s}\| = 0.18\pi \text{ (stopband cutoff frequency)} \qquad (10d)$$

the design procedure is illustrated below [22].

Step 1) Translate the filter specification of $H(w_1, w_2, w_3)$ to the specification of $H(w)$:
Given the 1-D filter specification: $\{\delta_p', \delta_s', w_p', w_s'\}$, the passband and stopband tolerances should follow $\delta_p' = \delta_p$ and $\delta_s' = \delta_s$, since the amplitude characteristics of $H(w)$ is preserved in $H(w_1, w_2, w_3)$. Determining the passband and stopband cutoff frequencies requires examination of the spherical surfaces defined in (10c) and (10d). For each

(w_{1p}, w_{2p}, w_{3p}) on the spherical surface defined in (10c), the corresponding 1-D frequency can be determined by $w_p' = \cos^{-1}[T(w_{1p}, w_{2p}, w_{3p})]$. The largest w_p' is chosen as the passband cutoff frequency of $H(w)$ such that the isopotential surface $\cos(w_p') = T(w_1, w_2, w_3)$ completely encircles the entire passband region. Similarly, the stopband cutoff frequency is the smallest value in the set of w_s' obtained from $w_s' = \cos^{-1}[T(w_{1s}, w_{2s}, w_{3s})]$, where the (w_{1s}, w_{2s}, w_{3s}) is any point on the spherical surface defined in (10d). This guarantees that the stopband region is completely outside the isopotential surface defined by $\cos(w_s') = T(w_1, w_2, w_3)$. As a result, a 1-D filter specified by the passband and stopband cutoff frequencies w_p' and w_s' will lead to a 3-D filter that meets the specification in the passband and stopband regions respectively. According to the approach described above, we obtained the 1-D filter specification: $\{\delta_p' = 0.134, \delta_s' = 0.030, w_p' = 0.08\pi, w_s' = 0.179\pi\}$.

Step 2) Design the 1-D filter that meets the specification obtained in Step 1:
The Parks-McClellan algorithm requires an order of at least 29 for the 1-D filter to meet the specification obtained in Step 1. A higher order of 31 was used in order to allow the possible deviation from the specification when transformed to the 3-D FIR filter.

Step 3) Determine the impulse response of the 3-D FIR filter:
From the 1-D filter $h[n]$ designed in Step 2 and the parameters of transformation function $t[n_1, n_2, n_3]$ illustrated in Fig. 1, we could determine the 3-D filter coefficients in $h[n_1, n_2, n_3]$ by using (1) and (4).

The resulting 3-D FIR filter retains the equiripple characteristic in $H(w)$. It can be observed from a 2-D slice of the frequency response $H(w_1, w_2, w_3)$, obtained by intersecting the (w_1, w_2, w_3)-space at $w_3 = 0$. As shown in Fig. 3, the magnitude response at the intersected (w_1, w_2)-plane is illustrated by a monochrome image, in which the brightest gray level corresponds to the maximum magnitude response and the darkest gray level corresponds to the minimum one. The equiripple phenomenon is apparent in the stopband region, yet it is unperceived in the passband region because of the very narrow passband width assumed in this particular example. Notice that the contours corresponding to $\cos(w) = T(w_1, w_2, w_3)$ deviate from spherical symmetry in the high-frequency regions (approximately $\|\overrightarrow{w}\| > 0.45\pi$), which does not substantially affect performance of the filter since those regions are outside the passband of the 3-D filter.

III. EEG MAPPING USING A 3-D FILTERING METHOD

An FIR filter can be implemented either by direct convolution or by using an fast Fourier transform (FFT) algorithm. In our study, it was found that the 3-D filtering process realized
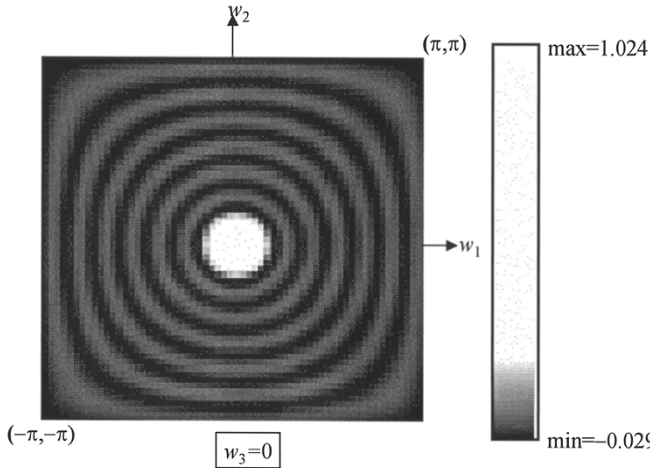
Fig. 3. A 2-D slice of the frequency response $H(w_1, w_2, w_3)$, obtained by intersecting the (w_1, w_2, w_3)-space at $w_3 = 0$.

Fig. 4. The potential value at site P is determined from the potential of the nearest electrode (Cz) at the preprocessing step.

by the FFT algorithm is more computationally efficient in comparison to realization by direct convolution. In addition, the former method is simple and straightforward to realize. In this manner, the constructed EEG mapping, $y[n_1, n_2, n_3]$, is obtained by computing the inverse Fourier transform of $\{H(w_1, w_2, w_3) \cdot X(w_1, w_2, w_3)\}$, where $X(w_1, w_2, w_3)$ is the Fourier transform of a 3-D input sequence $x[n_1, n_2, n_3]$. From the output sequence $y[n_1, n_2, n_3]$, we then extract output values at $[n_1, n_2, n_3]$ corresponding to the topographical coordinates of scalp surface for a final display of the interpolated EEG mapping. As a result, a merit of this proposed method is its capability of handling any irregular realistic head shape via a simple and straightforward way of data representation. In this preliminary study, we applied the spherical head model in compliance with the performance evaluation based on the spherical current dipole model. This filtering approach exploits the computational efficiency of FFT algorithms, together with the well-developed digital techniques.

One practical consideration is the preparation of the input pattern $x[n_1, n_2, n_3]$. Since only a few points of known (recorded) potential values are available, it requires a preprocessing step to assign values at the $[n_1, n_2, n_3]$'s ("cubes") near the scalp surface. Intuitively, the initialized input pattern does not significantly affect the output of the 3-D filter. To justify the hypothesis, we designed three approaches for preparing the input pattern. That is, the potential value at a nonrecording site $[n_1, n_2, n_3]$ was determined by: 1) the potential value of the nearest electrode site, 2) the average of potential values of the two nearest electrode sites, and 3) the average of potential values of the three nearest electrode sites. Then the three input patterns were processed by the 3-D filter to generate the EEG mappings. The deviation between two EEG mappings $y_1[n_1, n_2, n_3]$ and $y_2[n_1, n_2, n_3]$ was quantified by (11), shown at the bottom of the page, with N denoting the number of
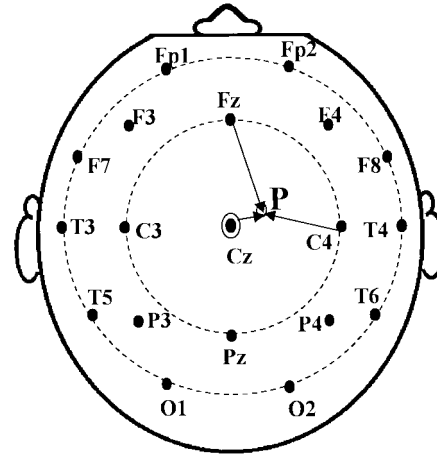
interpolated potential values (i.e., filter's output values) on the scalp. It was found in our experiment that the three input patterns initialized by the formulas given above resulted in the brain mappings with $dev\% < 5\%$. Therefore, the effect of the initialized input pattern on the EEG mapping is considered to be negligible in this study. We, thus, used the potential value of the nearest electrode site to fill up each cube. As is illustrated in Fig. 4, the potential value recorded at Cz is assigned to the site P, because Cz is the nearest electrode to site P. Regions away from the scalp surface have trivial effect on the scalp surface potential when performing the 3-D filtering.

The potential distribution on the scalp surface was simulated by the current dipole model consisting of a homogeneous sphere of neural tissue surrounded by two concentric shells of different electrical conductivities representing the skull and scalp [24], [25]. Consider a dipole source located near the center of the head (eccentricity $= 0.17$), with the negative polarity oriented toward $\vartheta = 35°$ (azimuth with respect to Cz) and $\varphi = 15°$ (longitude with respect to T4) [13]. The top view of the true potential distribution is shown in Fig. 5(a). Based on the 19-channel recording montage shown in Fig. 4, we extracted 19 potential values from the electrode sites. Applying a 3-D FIR filter with the filter specification given in (10), Fig. 5(b) displays the interpolated potential mapping. This mapping is similar in spatial frequency characteristics to the true one in Fig. 5(a), except that the centroid of the most negative region has moved to the right. Note that the range of the interpolated potential values differs from the one of the true values. While increasing the passband width $(\|\overrightarrow{w}_p\| = 0.40\pi)$, the interpolated potential mapping in Fig. 5(c) involves high-frequency components, which cause a spurious field distribution. From this mapping, we might misinterpret the location of the source. An inference may be drawn from this result, that is, a deep source generates on the

$$dev\% = \frac{\sqrt{\frac{1}{N}\sum_{[n_1,n_2,n_3]\in\text{scalp}}(y_1[n_1,n_2,n_3] - y_2[n_1,n_2,n_3])^2}}{\{\frac{1}{N}\sum_{[n_1,n_2,n_3]\in\text{scalp}}|y_1[n_1,n_2,n_3]|\}\{\frac{1}{N}\sum_{[n_1,n_2,n_3]\in\text{scalp}}|y_2[n_1,n_2,n_3]|\}} \times 100\% \qquad (11)$$
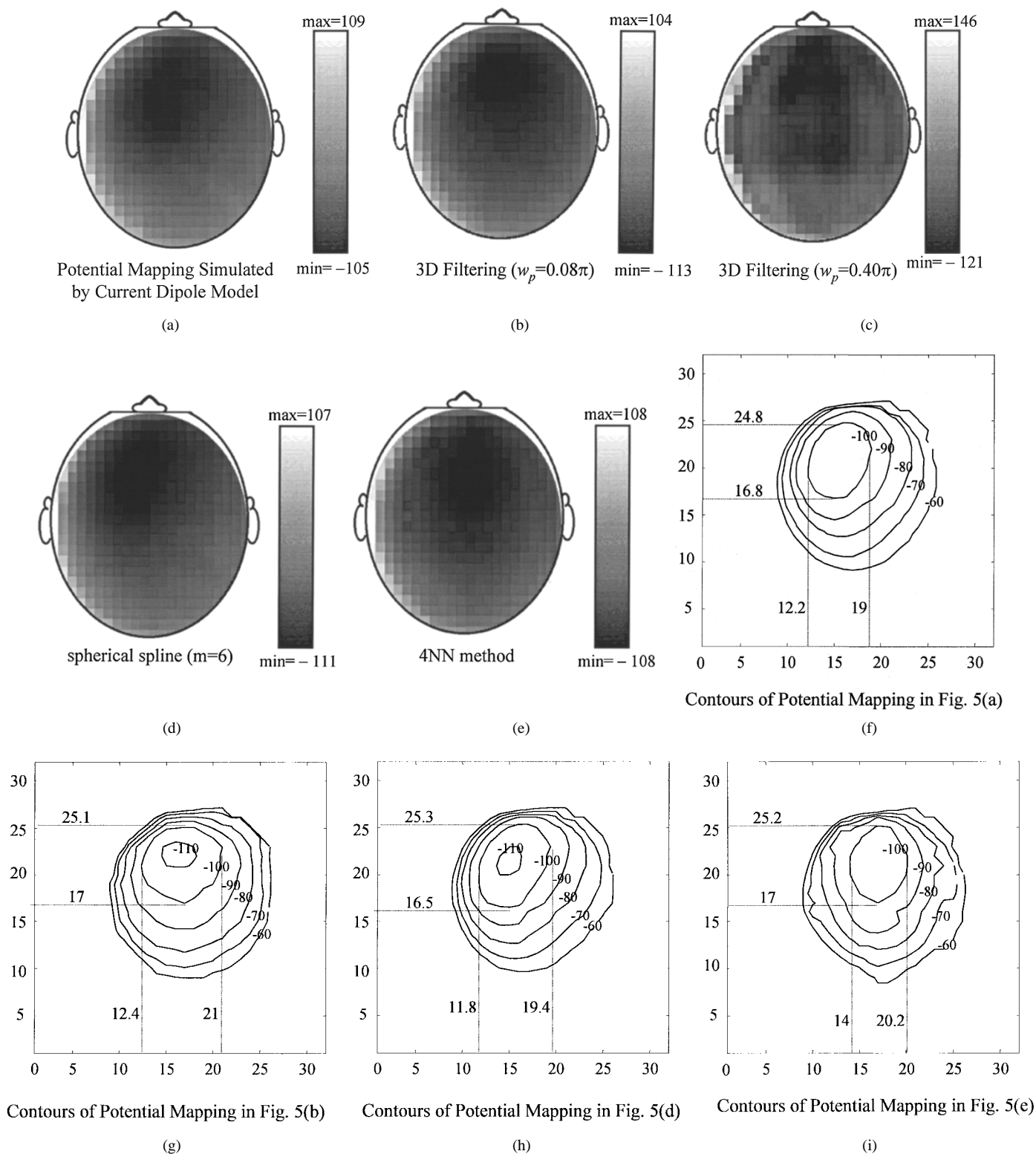
Fig. 5. The brain potential mapping (a) simulated by a current dipole model and (b)-(e) interpolated by different methods using 19 potential data points extracted from the simulated potential mapping in (a). The contours of the potential mappings in (a), (b), (d), and (e) were plotted in (f)–(i), respectively.

scalp surface a potential distribution with low spatial frequency characteristic. The surface potential varies at a slow gradient. An acceptable interpolation of the brain mapping can be obtained with a narrow-band low-pass filter (Fig. 3). Observing the brain mappings interpolated by the numerical methods [Fig. 5(d) and (e)], we found that the 4NN method, similar to the 3-D filtering method, resulted in a distorted potential mapping with the negative centroid transferring to the right. On visual inspection, the spherical splines method performed best among the three methods in this case study. The field distortion is more visible by examining the contour plots in Fig. 5(f)–(i), where the horizontal and vertical ranges of the

TABLE I
ELECTRODE SITES IN THE 19-, 33-, AND 45-ELECTRODE ARRAYS

19-electrode	The 19 electrode sites defined in Fig. 4.
33-electrode	Add 14 additional sites to the 19-electrode array: IO1 and IO2: infraorbital electrodes [33] MS1 and MS2: mastoid electrodes [33] CB1 and CB2: skull-base electrodes (insertions of sternocleidomastoid and trapezius muscles) [33] F5 (F6): mid-point electrode between F3 and F7 (F4 and F8) C1a (C2a): center of the quadrangle circumscribed by F3, Fz, Cz, and C3 (F4, Fz, Cz, and C4) C1p (C2p): center of the quadrangle circumscribed by P3, Pz, Cz, and C3 (P4, Pz, Cz, and C4) P5 (P6): mid-point electrode between P3 and T5 (P4 and T6)
45-electrode	Add 12 additional sites to the 33-electrode array: Fpz and Oz F3a (F4a): roughly mid-point electrode between Fp1 and F5 (Fp2 and F6) C5 (C6): mid-point electrode between C3 and T3 (C4 and T4) C5a (C6a): mid-point electrode between F5 and C5 (F6 and C6) Tcp1 (Tcp2): center of the quadrangle circumscribed by T3, C3, P3, and T5 (T4, C4, P4, and T6) P3p (P4p): roughly mid-point electrode between O1 and P5 (O2 and P6)

equipotential contours of -100 are labeled for comparison. According to the contour plots, the mapping generated by the 4NN method [Fig. 5(i)] deviates even more than the one generated by the 3-D filtering method [Fig. 5(g)] does from the true mapping [Fig. 5(f)]. Next, the error criterion in (11) is applied to evaluating the performance of different interpolation methods. We also analyze the efficiency of the three methods.

IV. COMPARISON OF PERFORMANCE AND EFFICIENCY

Based on the error criterion in (11), we evaluated the performance of the 3-D filtering method with different passband widths. The results were further compared to those of the 4NN and the spherical splines methods. This comparison was carried out for three common-reference recording montages including 19, 33, and 45 channels, respectively (Table I). In general, the 3-D filter is the low-pass type, of which the passband width depends on the spatial frequency characteristic of a potential mapping. Intuitively, the eccentricity of the dominant focal source determines the spatial frequency characteristic. A small eccentricity (a deep focal source) results in the surface potential varying at a slow gradient. As the eccentricity increases (the source focus moves toward the scalp), the potential distribution exhibits the characteristic of high spatial frequency. To address this issue, we first employed a 33-electrode array to investigate the effect of filter bandwidth (w_p) on the accuracy of interpolated potential mappings produced by the sources at different depths: the deep-region $(0 \leq$ eccentricity $\leq 0.3)$, mid-region $(0.3 \leq$ eccentricity $\leq 0.6)$, and shallow-region $(0.6 \leq$ eccentricity $\leq 0.8)$. In each region, 500 dipole sources were randomly generated. For each dipole source, the surface potential was first sampled by the 33-electrode array. From the 33 sampled

values, the interpolated potential mapping was constructed by the 3-D low-pass filter with passband width ranging from 0.03π to 0.30π. Then the normalized dev between the true and interpolated potential mappings was calculated.

Fig. 6 illustrates the dependence of the normalized dev on the passband width for the deep-region, mid-region, and shallow-region source foci. Each circle plotted in Fig. 6 indicates one dev value calculated from a simulated random dipole in the region under investigation. For comparison, the dev's for the spherical splines and 4NN methods are shown, respectively, by the diamond and plus symbols on the right. Given an w_p, the values of the dev demonstrate that a better performance can be obtained when the dipole sources are located in the deep region [Fig. 6(a)]. This is also the situation for the brain potential interpolation using the 4NN and spherical splines methods. The results are in agreement with intuitive reasoning. That is, the passband width needs to increase with increasing eccentricity to optimize the surface potential interpolation. Yet, the increase is very small. The smallest dev was obtained with $w_p = 0.12\pi$ in the deep and mid regions [Fig. 6(a) and (b)] and with $w_p = 0.13\pi$ in the shallow region [Fig. 6(c). The three solid curves in Fig. 6(d) plot the average dev (i.e., the average of 500 dev's evaluated from the 500 random dipoles) for each w_p in the three respective regions. The average dev's for the spherical splines and 4NN methods are denoted by the diamond and plus symbols, respectively. As illustrated in Fig. 6(d), the variation of dev is small for w_p ranging from 0.08π to 0.15π in the deep and middle regions and from 0.10π to 0.16π in the shallow region. This observation makes the application of the 3-D filtering method more feasible for the construction of EEG mappings. In fact, the accuracy of the 3-D filtering method
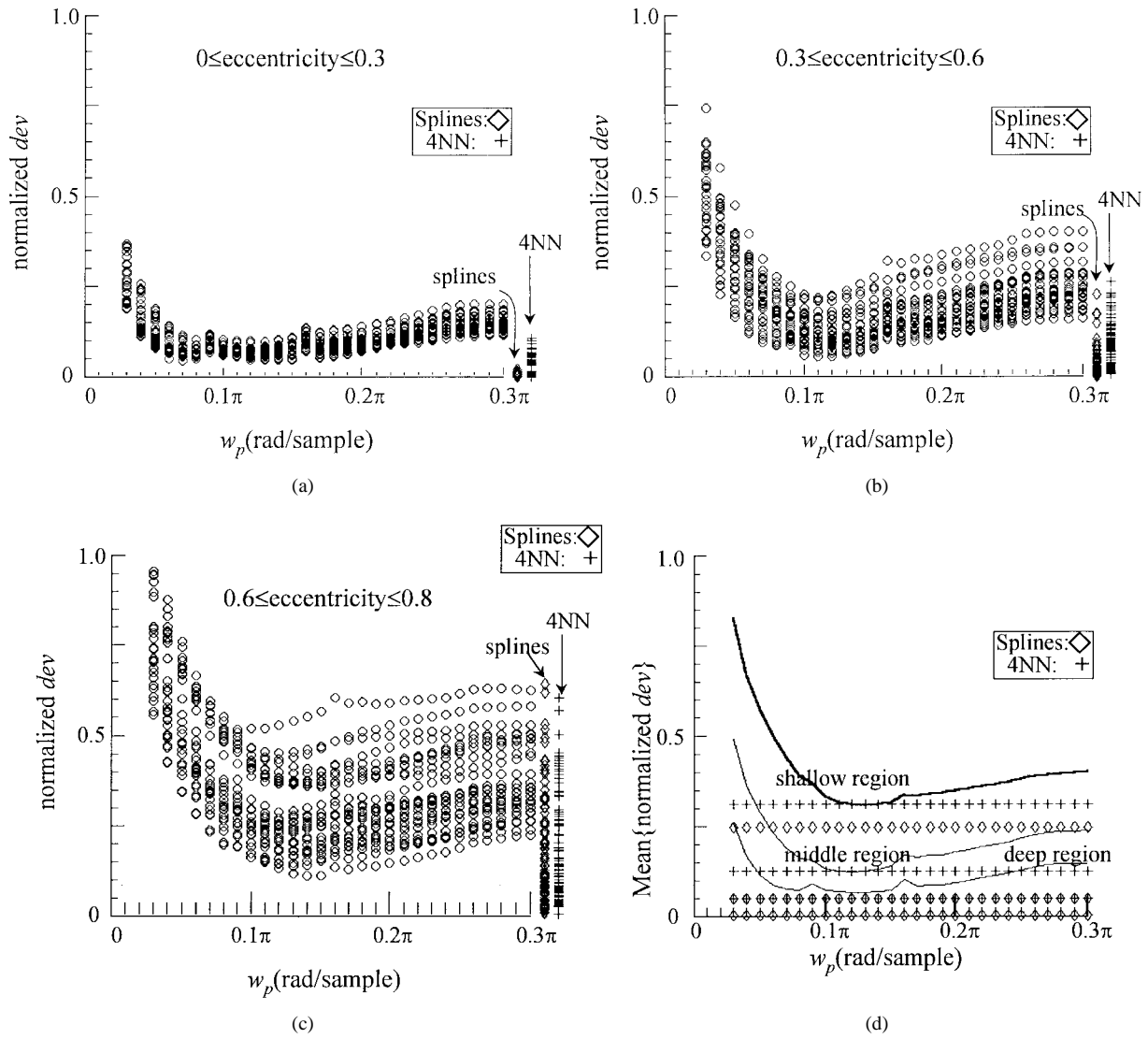
Fig. 6. The dependence of the normalized *dev* on the passband width $(0.03\pi \leq w_p \leq 0.3\pi)$ given the dipole sources located in (a) the deep region $(0 \leq \text{eccentricity} \leq 0.3)$, (b) the mid region $(0.3 \leq \text{eccentricity} \leq 0.6)$, and (c) the shallow region $(0.6 \leq \text{eccentricity} \leq 0.8)$. The *dev*'s evaluated for the spherical splines and 4NN methods are shown by the diamond $(\diamond)$ and plus $(+)$ symbols. Given an w_p, the average of the normalized *dev*'s (indicated by the circles) obtained by analyzing 500 randomly generated dipoles in each region is plotted in (d) for comparison.

highly depends on the origin of the focal source, instead of the passband width w_p. In general, we found that, for focal EEG activity, a passband width ranging from 0.08π to 0.15π resulted in a satisfactory interpolation for the scalp potential.

Next, the performance of the 3-D filtering method is compared to that of the 4NN and splines methods. Table II lists the average *dev*'s for the three methods based on the arrays of 19, 33, and 45 electrode sites. Note that, in the 3-D filtering method, the *dev* listed is the smallest one of all the average *dev*'s obtained with different w_p's. Accordingly, the value in parentheses indicates the corresponding (optimal) w_p. In the spherical splines method, a smaller m $(m = 3)$ is preferred for a higher number of recording electrodes. Apparently, the *dev*'s for the three methods increase with increasing eccentricity [Fig. 6(d) and Table II]. The spherical splines exhibits a consistent (with a small variance) and much superior performance in the deep region [Fig. 6(a)]. However, as the eccentricity increases, the performance becomes unpredictable.

In the shallow region, a larger variance of *dev*'s is observed for the spherical splines and 4NN methods [Fig. 6(c)]. Given an electrode-array size, the *dev*'s listed at the bottom (shaded area) of Table II are the average of *dev*'s in the three regions. The value quantifies the average performance of each method assuming that the source depth is unknown.

According to the quantitative error criterion in (11), the 3-D filtering method does not perform as well as the spherical splines. In comparison with the 4NN method, the 3-D filtering method demonstrates a competitive performance on the potential interpolation. Moreover, it is free from the problem of map discontinuities and extrema located at recording sites.

To evaluate the efficiency, the computation times required by the three methods were estimated for the arrays of 19, 33, and 45 electrode sites (Table I). A personal computer (Intel Pentium 133 MHz) was used to execute the interpolation task. The computation time was estimated from the average of the times required for reconstructing 500 different

TABLE II
PERFORMANCE COMPARISON—THE AVERAGE *dev*'s EVALUATED FOR THE THREE METHODS. THE VALUE IN
PARENTHESES IS THE PASSBAND WIDTH w_p THAT RESULTS IN THE BEST PERFORMANCE (THE SMALLEST *dev*)

Eccentricity of dipoles	Electrode array	3D filtering	4NN	Spherical splines (m=3)
0≤eccentricity≤0.3	19	0.07 (0.08π)	0.05	0.01
	33	0.07 (0.12π)	0.05	<0.01
	45	0.07 (0.13π)	0.04	<0.01
0.3≤eccentricity≤0.6	19	0.15 (0.10π)	0.16	0.10
	33	0.12 (0.12π)	0.13	0.05
	45	0.11 (0.12π)	0.10	0.03
0.6≤eccentricity≤0.8	19	0.38 (0.11π)	0.40	0.35
	33	0.31 (0.13π)	0.31	0.25
	45	0.28 (0.14π)	0.25	0.17
0≤eccentricity≤0.8	19	0.20	0.20	0.15
	33	0.17	0.16	0.10
	45	0.15	0.13	0.07

TABLE III
COMPUTATION TIME (IN s) REQUIRED BY DIFFERENT METHODS

	19-electrode array	33-electrode array	45-electrode array
3D Filtering Method	0.72	0.71	0.72
4NN method	0.36	0.47	0.60
Spherical Splines Method (m=3)	1.8	3.0	4.2

potential mappings. The 500 potential mappings were initially simulated by the current dipole model with its dipole source randomly generated. Each potential distribution was sampled with the three electrode arrays. We then applied one of the three algorithms to each set of sampled values to construct an interpolated potential mapping. For each algorithm, the times required for interpolating 500 potential mappings were averaged. The results are listed in Table III. Note that the computation time (approximately 0.7 s) required by the 3-D filtering method was independent of the number of electrodes. This is one of the advantages of applying the 3-D filtering method to the brain potential interpolation. On the other hand, the 4NN method needs longer execution time as the number of electrodes increases. Besides, in the 3-D filtering method, more than 60% of the computation time was spent on the evaluation of Fourier transforms, which can be accelerated by hardware realization. With the immense potential of the very powerful digital signal processors now available, we might be able to extend the current application of the 3-D filtering method to real-time animated potential mappings on a realistic head model.

V. DISCUSSION

This paper presents an alternative approach to reconstruction of the EEG topographical mapping on the scalp surface. As addressed in Section I, this research work was mainly motivated by the development of real-time animated displays of EEG mappings which might be realized and implemented by hardware based on the digital filtering technique. As far as the author is aware, it is the first attempt to interpolate the EEG mapping using a filtering approach, other than the commonly used numerical interpolation algorithms. Therefore, the author paid special attention in illustrating the method and relevant details of implementation.

According to visual inspection, the potential mapping interpolated by the 3-D filtering method has a quality comparable to that obtained by the 4NN and spherical splines methods. Based on the quantitative error criteria in (11), the performance of the 3-D filtering method compares well with the commonly used 4NN method. In comparison with the spherical splines method, the potential mapping interpolated by the 3-D filtering method deviates more from the true mapping due to the alteration

of the true potential values, by the filtering process, at the recording sites.

The 3-D filtering method provides an engineering means of interpolating scalp potential data, which are treated as a 3-D signal. In comparison with the spherical splines method, the computational efficiency of the proposed method can be highly improved with the aid of digital technology. Particularly, the filter can be implemented in the frequency domain, fully utilizing the computational efficiency of the FFT. The computational efficiency is particularly emphasized because of our intention of developing real-time animated brain potential mappings.

Representation of the potential values by a 3-D signal model $x[n_1, n_2, n_3]$, in addition, provides a simple medium for 3-D display of brain potential distribution on an anatomically realistic head. By discretization, we can determine the coordinate $[n_1, n_2, n_3]$ of any location on the scalp of an irregular realistic head. Since the 3-D filtering process can be performed on any 3-D signal, no constraint is imposed in the head shape. Further work toward a realistic head model on the basis of a higher number of recording sites has been under way.

References

[1] T. Kalayci and Ö. Özdamar, "Wavelet preprocessing for automated neural network detection of EEG spikes," *IEEE Eng. Med. Biol. M*, vol. 14, no. 2, pp. 160–166, 1995.

[2] R. Cooper, J. W. Osselton, and J. C. Shaw, *EEG Technology*, 3rd ed. Woburn, MA: Butterworth, 1980.

[3] T. Estrin and R. Uzgalis, "Computerized display of spatio-temporal EEG patterns," *IEEE Trans. Biomed. Eng.*, vol. BME-16, pp. 192–196, 1969.

[4] M. R. Nuwer, "Quantitative EEG: I. Techniques and problems of frequency analysis and topographic mapping," *J. Clin. Neurophys.*, vol. 5, pp. 1–43, 1988.

[5] D. Lehmann, "Past, present and future of topographic mapping," *Brain Topogr*, vol. 3, no. 1, pp. 191–202, 1990.

[6] P. L. Nunez, R. B. Silberstein, P. J. Cadusch, and R. Wijesinghe, "Comparison of high resolution EEG methods having different theoretical bases," *Brain Topogr*, vol. 5, no. 4, pp. 361–364, 1993.

[7] A. S. Gevins, N. H. Morgan, S. L. Bressler, B. A. Cutillo, R. M. White, J. Illes, D. S. Greer, J. C. Doyle, and G. M. Zeitlin, "Human neuroelectric patterns predict performance accuracy," *Sci*, vol. 235, pp. 580–585, 1987.

[8] A. S. Gevins, P. Brickett, B. Costales, J. Le, and B. Reutter, "Beyond topographic mapping: Toward functional-anatomical imaging with 124-channel EEG's and 3-D MRI's," *Brain Topogr.*, vol. 3, no. 1, pp. 53–64, 1990.

[9] L. Soufflet, M. Toussaint, R. Luthringer, J. Gresser, R. Minot, and J. P. Macher, "A statistical evaluation of the main interpolation methods applied to three-dimensional EEG mapping," *Electroenceph. Clin. Neurophys.*, vol. 79, pp. 393–402, 1991.

[10] A. B. Barreto, J. C. Principe, and S. A. Reid, "STL: A spatio-temporal characterization of focal interictal events," *Brain Topogr.*, vol. 5, no. 3, pp. 215–228, 1993.

[11] D. A. Shepard, "A two-dimensional interpolation function for irregular-spaced data," in *Proc. ACM Nat. Conf.*, 1968, pp. 517–524.

[12] M. S. Buchsbaum, F. Rigal, R. Coppola, J. Cappelletti, C. King, and J. Johnson, "A new system for gray-level surface distribution maps of electrical activity," *Electroenceph. Clin. Neurophys.*, vol. 53, pp. 237–242, 1982.

[13] F. Perrin, J. Pernier, O. Bertrand, M. H. Giard, and J. F. Echallier, "Mapping of scalp potentials by surface spline interpolation," *Electroenceph. Clin. Neurophys.*, vol. 66, pp. 75–81, 1987.

[14] F. Perrin, O. Bertrand, and J. Pernier, "Scalp current density: Value and estimation from potential data," *IEEE Trans. Biomed. Eng.*, vol. BME-34, pp. 283–288, 1987.

[15] F. Perrin, J. Pernier, O. Bertrand, and J. F. Echallier, "Spherical splines for scalp potential and current density mapping," *Electroenceph. Clin. Neurophys.*, vol. 72, pp. 184–187, 1989.

[16] G. Wahba, "Spline interpolation and smoothing on the sphere," *SIAM J. Sci. Stat. Comput.*, vol. 2, no. 1, pp. 5–16, 1981.

[17] F. H. Duffy, J. F. Burchfield, and C. T. Lombroso, "Brain electrical activity mapping (BEAM): A method for extending the clinical utility of EEG and evoked potential data," *Ann. Neurol.*, vol. 5, pp. 309–321, 1979.

[18] H. Ashida, J. Tatsuno, J. Okamota, and E. Maru, "Field mapping of EEG by unbiased polynomial interpolation," *Comput. Biomed. Res.*, vol. 17, pp. 267–276, 1984.

[19] Z. J. Koles, A. Kasmia, R. B. Paranjape, and D. R. McLean, "Computed radial-current topography of the brain: Patterns associated with the normal and abnormal EEG," *Electroenceph. Clin. Neurophys.*, vol. 72, pp. 41–47, 1989.

[20] S. K. Law, P. L. Nunez, and R. S. Wijesinghe, "High-resolution EEG using spline generated surface Laplacians on spherical and ellipsoidal surfaces," *IEEE Trans. Biomed. Eng.*, vol. 40, pp. 145–153, Feb. 1993.

[21] T. F. Oostendorp and A. van Oosterom, "The surface Laplacian of the potential: Theory and application," *IEEE Trans. Biomed. Eng.*, vol. 43, pp. 394–405, Apr. 1996.

[22] J. S. Lim, *Two-Dimensional Signal and Image Processing*. Englewood Cliffs, NJ: Prentice-Hall, 1990.

[23] M. Schneider, "A multistage process for computing virtual dipolar sources of EEG discharges from surface information," *IEEE Trans. Biomed. Eng.*, vol. BME-19, pp. 1–12, 1972.

[24] J. P. Ary, S. A. Klein, and D. H. Fender, "Location of sources of evoked scalp potentials: Corrections for skull and scalp thicknesses," *IEEE Trans. Biomed. Eng.*, vol. BME-28, pp. 447–452, 1981.

[25] R. P. Gaumond, J. H. Lin, and D. B. Geselowitz, "Accuracy of dipole localization with a spherical homogeneous model," *IEEE Trans. Biomed. Eng.*, vol. BME-30, pp. 29–34, 1983.

[26] J. H. McClellan, "The design of two-dimensional digital filters by transformation," in *Proc. 7th Annu. Princeton Conf. Inform. Sci. Syst.*, 1973, pp. 247–251.

[27] R. M. Mersereau, W. F. G. Mecklenbrauker, and T. F. Quatieri Jr., "McClellan transformations for two-dimensional digital filtering: I. Design," *IEEE Trans. Circuits Syst.*, vol. CAS-23, pp. 405–414, 1976.

[28] J. H. McClellan and D. S. K. Chan, "A 2-D FIR filter structure derived from the Chebyshev recursion," *IEEE Trans. Circuits Syst.*, vol. CAS-24, pp. 372–378, 1977.

[29] R. M. Mersereau, "The design of arbitrary 2-D zero-phase FIR filters using transformations," *IEEE Trans. Circuits Syst.*, vol. CAS-27, pp. 142–144, 1980.

[30] D. E. Dudgeon and R. M. Mersereau, *Multidimensional Digital Signal Processing*. Englewood Cliffs, NJ: Prentice-Hall, 1984.

[31] J. H. McClellan and T. W. Parks, "A unified approach to the design of optimum FIR linear phase digital filters," *IEEE Trans. Circuit Theory*, vol. CT-20, pp. 697–701, Nov. 1973.

[32] J. H. McClellan, T. W. Parks, and L. R. Rabiner, "A computer program for designing optimum FIR linear phase digital filters," *IEEE Trans. Audio Electroacoust.*, vol. AU-21, pp. 506–526, Dec. 1973.

[33] F. Matsuo, "Expanded head surface EEG electrode array: An application to display the voltage topography of focal epileptiform discharges of mesiotemporal origin," *J. Clin. Neurophysiol.*, vol. 8, no. 4, pp. 442–451, 1991.

Pei-Chen Lo (S'88–M'89) was born in Taiwan on November 5, 1962. She received the B.S. degree in electrical engineering from National Tsing-Hua University, Taiwan, in 1984, and the Ph.D. degree, specializing in EEG signal analysis, in electrical engineering from the University of Florida, Gainesville, in 1990.

From 1990 to 1992, she was a Research Associate in the EEG laboratory, University of Utah Medical Center, Salt Lake City. She is currently an Associate Professor in the Department of Electrical and Control Engineering, National Chiao Tung University, Hsinchu, Taiwan. Her research interests include signal processing and digital technologies applied to the biomedical field.